

A Model for the Solubility of Anhydrite in H₂O-NaCl fluids from 25 to 800 °C, 0.1 to 1400 MPa, and 0 to 60 wt% NaCl: Applications to Hydrothermal Ore-forming Systems

by

Emily C. Creaser

A thesis submitted in partial fulfillment of the requirements for the degree of

Master of Science

Department of Earth and Atmospheric Sciences

University of Alberta

Abstract

Anhydrite (CaSO_4) is a common gangue mineral in hydrothermal ore-forming systems, though currently there is no robust numerical model for the solubility of anhydrite in H_2O -NaCl hydrothermal fluids. Here, we present a thermodynamic model for the solubility of anhydrite in saline aqueous fluids for a broad range of pressures, temperatures, and fluid salinities. The generalized solubility model is adapted from Brooks and Steele-MacInnis (2019), which is a combined approach of the previous solubility models of Akinfiyev and Diamond (2009) and of Dolejš and Manning (2010). A dataset of experimentally determined solubilities for anhydrite was used to calibrate the model, and the experimental data covers P-T-X ranges of 0.1 - 1400 MPa, 25 - 800 °C, and 0 - 60 wt% NaCl. The model is successful at reproducing solubility values and overall trends from the experimental dataset within error, and is also capable of reproducing results for experimental solubility data that was purposefully not included in model calibration. We demonstrate that this solubility model can perform well over a wide-range of P-T-X conditions, including conditions of liquid + vapor coexistence. We also show that the solubility model is a robust tool that can be used to predict the potential precipitation and/or dissolution of anhydrite along representative fluid flow paths within various hydrothermal systems.

Preface

Chapters 1 - 5 have been submitted for publication in Chemical Geology as of August 4th 2021, co-authored by myself, Matthew Steele-MacInnis, and Benjamin M. Tutolo. I was responsible for the calibration and application of the solubility model, as well as manuscript composition. Matthew Steele-MacInnis was the supervisory author and was involved with manuscript composition and the development of this thesis project. Benjamin M. Tutolo assisted with manuscript feedback and edits.

Acknowledgements

I would like to thank Matthew Steele-MacInnis for his guidance and enthusiasm while supervising my research, his advice and teachings have been wholly appreciated these past two years. I am grateful to Pilar Lecumberri-Sanchez for sitting on my supervisory committee and for providing valuable feedback during the development of this project. Many thanks to Yuri Klyukin for his numerical model program on the thermodynamic properties of H₂O-NaCl fluids, it was a valuable tool during my research. I appreciate the helpful feedback and edits provided by Ben Tutolo during the submission process. I gratefully acknowledge that this work was supported by NSERC through a Discovery grant to Matthew Steele-MacInnis. Thank you to J.M and to my family for their continued support throughout both my undergraduate and graduate degrees.

Table of Contents

Abstract	ii
Preface	iii
Acknowledgements	iv
List of Tables	vi
List of Figures	vi
1. Introduction	1
1.1 Anhydrite in Hydrothermal Ore-Forming Systems	3
1.2 Solubility models for common gangue minerals	6
2. Methods and Calibration of Solubility Model	9
2.1. Sources of Experimental Data	9
2.2. Calculations of Fluid Properties	10
2.3. Calibration of the Solubility Model	10
3. Results	11
3.1 Solubility Model and Goodness of Fit	11
3.2 Effects of Pressure, Temperature, and Salinity	12
3.3. Solubility of Anhydrite under Conditions of Liquid-Vapor Immiscibility	14
4. Discussion	15
4.1. Major Controls on Anhydrite Solubility	15
4.2. Example Applications to Hydrothermal Ore-Forming Systems	17
4.2.1 Applications to VMS deposits and active sub-seafloor hydrothermal systems	17
4.2.2 Applications to Porphyry copper deposits	18
5. Conclusions	20
References	21
Tables	28
Figures	29

List of Tables

Table 1.....	28
Table 2.....	28

List of Figures

Figure 1.....	29
Figure 2.....	30
Figure 3.....	31
Figure 4.....	32
Figure 5.....	33
Figure 6.....	34
Figure 7.....	35
Figure 8.....	36
Figure 9.....	37

1. Introduction

Sulfur plays multiple crucial roles in the formation of hydrothermal mineral deposits. Sulfur species in aqueous solution commonly serve as ligands for transporting various metals in hydrothermal fluids (Seward et al. 2014), and strongly affect both the solubility of metals and their partitioning between aqueous fluids and silicate melts (Zajacz et al. 2017), and between aqueous liquid and vapor (Williams-Jones and Heinrich 2005, Pokrovski et al. 2008). Both reduced (S^{2-}) and oxidized (S^{6+}) sulfur ions are basic constituents of both common ore (sulfide) minerals and gangue (sulfate) minerals. Aqueous species of both the latter ions take part in pH-dependent reactions, such as equilibria between HS^- and H_2S and between SO_4^{2-} and HSO_4^- . Moreover, redox equilibria between reduced and oxidized sulfur are instrumental to numerous processes of oxidation and reduction in ore-forming settings. Stable isotopes of sulfur are commonly used to trace the sources of ore-forming fluids as well as fluid-rock reactions and redox processes that affect ore formation (Ohmoto 1972). Sulfur-bearing gangue minerals, such as anhydrite, are also commonly observed in close association with ore mineralization in hydrothermal settings (Lowell et al. 2003, Sillitoe 2010, Henley et al. 2015, Tornos et al. 2016). Hence, the factors that control precipitation and dissolution of sulfate gangue minerals in these settings are critical to deciphering hydrothermal ore-forming processes.

Solubility models for quartz in hydrothermal settings have contributed to our understanding of ore-forming processes in a variety of ways. For example, modeling the aqueous transport of silica and precipitation of quartz in response to boiling in the H_2O system has provided insight into formation of epithermal precious metal deposits (Cline et al. 1992). Extension of similar modeling of quartz dissolution and precipitation in the H_2O -NaCl system

enabled new insights into the distribution of quartz veins and their fluid inclusion types in mid-ocean ridge hydrothermal systems and volcanogenic massive-sulfide (VMS) deposits (Steele-MacInnis et al. 2012a, b), and in magmatic-hydrothermal settings that form porphyry-type ore deposits (Monecke et al. 2018, Sun et al. 2021). Further extension to the system $\text{H}_2\text{O}-\text{NaCl}-\text{CO}_2$ has also added insight into porphyry vein formation (Monecke et al. 2019) and has allowed for modeling quartz deposition in orogenic Au veins (Li et al. 2020). These applications have shown that a thermodynamic model for the solubility of quartz can provide valuable insights into the factors controlling vein formation. The goal of this present study is to develop and apply an analogous model for the solubility of anhydrite.

Anhydrite (CaSO_4) is a common gangue mineral and commonly found in close paragenetic association with sulfide ore minerals in a variety of hydrothermal systems types. Anhydrite is a well-known vein mineral especially in porphyry-Cu and VMS deposits, and is also common and abundant in iron oxide - apatite (IOA) deposits and REE-bearing carbonatites. However, despite the important role that the precipitation of anhydrite plays in these deposits, there is currently no comprehensive numerical model for the solubility of anhydrite in saline hydrothermal fluids over a wide range of pressures and temperatures. Anhydrite solubility in relatively dilute aqueous solutions can be estimated using the Helgeson-Kirkham-Flowers equation of state (Helgeson et al. 1976, 1981) as implemented in SUPCRT92 (Johnson et al. 1992), but this model is limited to fluids of liquid-like density and relatively low salinities. Hence, applications to systems that involve high-salinity brines and/or liquid-vapor immiscibility are limited. Here, we outline the calibration of a new thermodynamic model for the solubility of anhydrite in saline hydrothermal fluids over wide ranges of pressure, temperature, and salinity.

We show how this model can be applied to predict the potential dissolution and precipitation of anhydrite in hydrothermal systems.

1.1 Anhydrite in Hydrothermal Ore-Forming Systems

Anhydrite is a common gangue mineral in many hydrothermal ore-deposit types, including porphyry (Henley et al. 2015, Sykora et al. 2018, Hutchinson and Dilles 2019); VMS as well as active submarine hydrothermal vents (Pujatti et al. 2021); IOA (Bain et al. 2020, 2021); rift-related vein deposits (Walter et al. 2018), as well as numerous hydrothermal ore types associated with carbonatitic magmatism (Walter et al. 2021). In many of these deposits, anhydrite is intimately associated with metal sulfide and/or oxide mineralization. Anhydrite is commonly the dominant or sole sulfate mineral present in many such hydrothermal ore deposits. Hence, modeling the solubility of anhydrite in these systems can provide insight into the geochemical behaviour of sulfate and its role in hydrothermal ore formation.

Porphyry copper deposits can be categorized as massive sulfur anomalies (Blundy et al. 2015). In these deposits, anhydrite is a common gangue mineral that occurs in veins and as part of hydrothermal alteration assemblages (Sillitoe 2010, Cooke et al. 2014). Mineral inclusions of anhydrite are also commonly observed in igneous phenocrysts sourced from porphyry copper deposits, suggesting that these magmas are anhydrite saturated (Hutchison and Dilles 2019), and a role of sulfate-rich melts in such settings is increasingly recognized (Hutchison et al. 2020). Deposition of anhydrite in hydrothermal veins is promoted by disproportionation of magmatic SO_2 which generates H_2S and H_2SO_4 . Reduced sulfur (H_2S) produced by this reaction forms hydrosulfide complexes with Au and Cu (Zajacz et al., 2010, 2017) and enables deposition of sulfide minerals (Henley et al. 2015). Meanwhile, H_2SO_4 reacts with Ca-bearing feldspars in the wall rock to form anhydrite (Cooke et al. 2014, Henley et al. 2015) and gives rise to acid-sulfate

alteration in the shallower epithermal environments (Rye et al. 1992). In some cases, anhydrite is deposited as a gangue mineral in high-sulfidation epithermal veins (Hedenquist et al. 2017), whereas in other cases the dissolution of earlier-formed anhydrite creates fluid-flow pathways that promote epithermal mineralization (Sykora et al. 2018). Hence, anhydrite deposition and dissolution in these settings is intimately associated with hydrothermal alteration and ore formation (Henley et al. 2015). Anhydrite solubility also plays a role in the later (post-mineralization) stages of fluid circulation, when dissolution of anhydrite by lower-temperature surface water can lead to disintegration of the altered rock (Sillitoe 2020).

Sulfate is the second most abundant anion in seawater, and anhydrite is common in both active submarine hydrothermal systems and in their fossil analogs, the VMS deposits. At active spreading centres, such as at the East Scotia Ridge and the TAG hydrothermal mound, anhydrite deposition is intimately associated with sulfide minerals at chimneys and in stock-work veins (Tivey et al. 1995, Petersen et al. 2000, Lowell et al. 2003, James et al. 2014, Pujatti et al. 2021). Studies of anhydrite hosted fluid inclusions in these systems provide evidence for phase separation that occurs in sub-seafloor environments (Nehlig 1991). As cool seawater is drawn into hydrothermal systems at spreading centers, anhydrite is expected to precipitate as a result of the retrograde temperature dependence of the solubility of anhydrite (Lowell et al. 2003). Similarly, mixing of relatively cool seawater with ascending hydrothermal fluids at temperatures above 150°C is expected to trigger anhydrite precipitation (Pujatti et al. 2021) and may form an impermeable barrier that segregates the fluid flow paths that vent diffuse, low temperature fluids versus those that feed focused, high temperature fluid discharge (Lowell et al. 2003). Fluid mixing, coupled with retrograde temperature dependence of solubility and redox reactions between relatively oxidized seawater and reduced hydrothermal fluid, gives rise to a variety of

replacement reactions and a close paragenetic association between anhydrite and sulfide minerals in these settings (Pujatti et al. 2021).

In sedimentary basins and continental rift settings, sulfate-rich basinal brines play major roles in the formation of hydrothermal ore deposits (Walter et al. 2017, 2018) and anhydrite serves as both a sulfate source and a common gangue mineral. For example, rift-related veins in the Schwarzwald district of Germany record mixing of fluids derived from multiple aquifers, with variable concentrations of sulfate depending on the presence of gypsum/anhydrite evaporites (Walter et al. 2017, 2018). Similarly, fluid mixing involving sulfate-bearing brines is a commonly invoked trigger for sulfide mineralization in MVT deposits (Leach et al. 2005). For example, at Pine Point (NWT) in Canada, precipitation of coarse sphalerite was enabled when aqueous sulfate in the metal-bearing brine was to sulfide by mixing with petroleum (Szmihelsky et al. 2021). Sulfate in the ore-forming brine was most likely sourced from Devonian anhydrite-rich evaporites deposited in the back-reef environment adjacent to the mineralized platform carbonates (Szmihelsky et al. 2021).

The nature of the ore-forming fluids responsible for forming IOA deposits is controversial, but recent studies increasingly point to a key role of sulfate-rich fluids (Bain et al. 2020, 2021). At El Laco, Chile, anhydrite occurs as veins, mounds, and alteration zones commonly associated with magnetite ore, and is also observed within fluid and melt inclusions (Broman et al. 1999, Tornos et al. 2016, Bain et al. 2021), suggesting that sulfate-rich fluids play a role in iron-ore mineralization (Tornos et al. 2016, 2017). Similarly, fluid inclusion assemblages in apatite and actinolite from IOA deposits at Buena Vista (Nevada) and Iron Springs (Utah) show evidence for sulfate-bearing or even sulfate-dominant ore forming fluids (Bain et al. 2020).

Sulfate-bearing and sulfate-rich fluids are also common in carbonatites and their associated hydrothermal systems (Walter et al. 2021). For example, fluid inclusions associated with the carbonatitic magmatism associated with the Kaiserstuhl in Germany contain sulfate concentrations up to tens of wt% (Walter et al. 2020). Complex, multi-component fluid inclusions in such settings commonly contain sulfate daughter minerals including anhydrite (Walter et al. 2020). Sulfate rich fluids in these systems can be efficient agents to transport rare-Earth elements (REE) and likely influence REE mineralization in systems related to carbonatite melts (Cui et al. 2020).

1.2 Solubility models for common gangue minerals

Solubility models can be broadly subdivided into electrostatic-type models and models based on fluid density (Dolejš 2013). The electrostatic-type models, such as the (revised) Helgeson-Kirkham-Flowers equation of state (Helgeson et al. 1981, Tanger and Helgeson 1988), have the advantage of enabling predictive modeling of homogeneous equilibria between species in aqueous solution, but tend to be limited to restricted regions of pressure-temperature space. Density-based models, in contrast, provide less information on aqueous species, but can be calibrated to encompass much wider ranges of pressure and temperature, including both liquid-like and vapor-like densities and from pure H₂O to highly saline brines (Manning 1994, Dolejš and Manning 2010, Brooks and Steele-MacInnis 2019). Hybrid approaches that perform density-based extrapolations using calculations based on electrostatic models (e.g., Scheuermann et al. 2019) have also been presented, but have not been widely tested. The present contribution takes a density-based approach.

The density-based family of solubility models take the general form of correlating the apparent equilibrium constant, K , of the dissolution reaction with density of the solvent. This

correlation is rooted in the empirical observation that free energies of solvation tend to scale with the logarithm of the solvent density (Marshall and Quist 1967, Dolejš 2013). A correlation equation of this type was developed for quartz solubility in H₂O by Fournier and Potter (1982), and was extended to H₂O-NaCl solutions by Fournier (1983). However, the latter models were purely empirical in form and involved at least eight fitting parameters, rendering these equations unsuitable to extrapolation over wide ranges of pressure, temperature, and fluid composition. Manning (1994) developed an improved model for the solubility of quartz in H₂O of the form $\log K = A(T) + B(T)\log\rho$, where $A(T)$ and $B(T)$ are polynomial equations in temperature and ρ represents density of H₂O. This model was highly successful in representing quartz solubility over a wide range of pressure and temperature from ambient surface conditions through to the lower crust and upper mantle (Manning 1994). This equation was extended to saline fluids by Akinfiyev and Diamond (2009) using an approach similar to that of Fournier (1983).

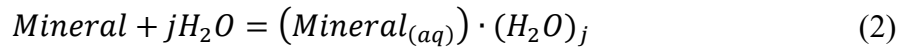
The model by Dolejš and Manning (2010) refined the form of the equation to align with the virial expansion of the solvation free energy, according to:

$$-RT\ln K = a + bT + cT\ln T + dT^2 + eT\ln\rho \quad (1)$$

Here, T is temperature (Kelvin), R is the gas constant ($8.314 \text{ J mol}^{-1} \text{ K}^{-1}$), ρ is solvent (H₂O) density (g cm^{-3}), and parameters a through e are mineral-specific fitting coefficients (Dolejš and Manning 2010). In the case of mineral dissolution in pure H₂O, and assuming unit activity coefficients, the apparent equilibrium constant K is commensurate to the molal solubility, $\ln K = \ln m_{\text{mineral}}$. The model was calibrated based on experimental data for solubility of quartz, corundum, rutile, fluorite, portlandite, and fluoroapatite over a wide range of pressures and

temperatures (Dolejš and Manning 2010). For several of these minerals, coefficients c and d were set to zero, such that the equation invokes only three or five fitting parameters depending on the mineral in interest.

Brooks and Steele-MacInnis (2019) extended the model of Dolejš and Manning (2010) to H₂O-NaCl fluids. In this model, the solubility of each mineral in H₂O-NaCl fluids is represented by the sum of a two-step process of the form:



In equations 2 and 3, parameters j and q are bulk stoichiometric coefficients, which are optimized during fitting. The apparent equilibrium constants for these two reactions are termed K_1 and K_2 , respectively. These parameters are fitted sequentially based on experimental solubility data for each mineral in H₂O and H₂O-NaCl solutions using a modified version of Eq. (1) in which ρ is substituted by ρ^* , termed the effective density of the fluid and calculated according to:

$$\rho^* = \frac{18.0152}{x_{\text{H}_2\text{O}} V_{\text{mix}}} \quad (4)$$

Where $x_{\text{H}_2\text{O}}$ is the mole fraction of H₂O and V_{mix} is the molar volume of the fluid (cm³ mol⁻¹).

The solubility of a mineral is then the sum of species produced by the two-step process represented by Eqs. (2) and (3), and given by:

$$m_{Mineral} = K_1 x_{H_2O}^j + K_1 K_2 x_{H_2O}^j m_{NaCl}^q \quad (5)$$

2. Methods and Calibration of Solubility Model

2.1. Sources of Experimental Data

We compiled a comprehensive database of experimental data for the solubility of anhydrite in H₂O-NaCl fluids (Table 1). These studies cover a broad range of pressures, temperatures, and salinities from 0.1 to 1400 MPa, 25 to 800 °C, and 0 to 58 wt% NaCl (Table 1). Several studies were conducted at ambient pressure of 0.1 MPa using standard wet-chemistry techniques (Madgin & Swales 1956, Bock 1961, Block & Waters 1968, Glew & Hames 1970). Higher pressure-temperature experiments were done using various types of pressure vessels/autoclaves (Marshall et al. 1964, Templeton and Rodgers 1967, Blount & Dickson 1969) and the high-pressure experiments of Newton and Manning (2005) were done using a piston cylinder. The total range in anhydrite solubility documented by these studies varies over five orders of magnitude (in molal units), and both the specific values and the overall trends with pressure, temperature, and salinity are broadly consistent between all studies. Overall, the experimental data indicate that anhydrite solubility increases with increasing pressure; first decreases but then increases with increasing temperature (i.e., shows both retrograde and prograde temperature dependence of solubility): and increases strongly with increasing salinity (i.e., shows strong salting-in). Furthermore, the recent study by Scheuermann et al. (2019) documents variation in anhydrite solubility with fluid density in the vapor phase. The latter study was not included in the regression analysis, but was used to test the validity and extrapolation of the model.

2.2. Calculations of Fluid Properties

Calculations of fluid properties were done using the computer program of Klyukin et al. (2020). Within this program, the density of H₂O fluid was calculated using the IAPWS-95 equation of state of Wagner and Pruß (2002). Fluid phase equilibria, including vapor pressure and salinities of immiscible liquid and vapor in the system H₂O-NaCl were modeled according to the equations of Driesner and Heinrich (2007). Densities of H₂O-NaCl fluids were calculated using equations of Driesner (2007).

2.3. Calibration of the Solubility Model

The first step of the calibration was to fit the equation for K_1 according to Eq. (1) based on the experimental data for solubility of anhydrite in pure H₂O by multiple-linear regression. In this step, we used the full five-parameter form of Eq. (1) with coefficients a through e . The experimental values for K_1 from the literature were obtained according to $K_1 = m_{\text{anhydrite}}$ in pure H₂O. Note that the stoichiometric coefficient j is not yet modeled in this first step and is instead optimized in the second step according the solubility of anhydrite in saline fluids (see Brooks and Steele-MacInnis 2019). The fitted coefficients for the K_1 equation are listed in Table 2 and represent our solubility model for anhydrite in pure H₂O.

The second step in the analysis is to fit the coefficients for the K_2 equation, as well as the stoichiometric coefficients j and q , based on the solubility data for H₂O-NaCl fluids. To do so, we start by computing K_1 at the conditions of each experiment using the fitted parameters obtained in the previous step. Next, we rearrange Eq. (5) to solve for the value of K_2 implied by each experimental data point (in effect, according to the difference between the experimental solubility in H₂O-NaCl fluids, versus the predicted solubility in pure H₂O at equivalent P and T), using preliminary values for j and q (which are optimized in the final step). We fit the

coefficients for K_2 by multiple-linear regression using the simplified, three-parameter version of Eq. (1). Finally, we optimize the values for the stoichiometric coefficients j and q by iterative refinement in order to minimize the global root-mean-squared deviation (RMSD). The derived coefficients (a , b , and e in the equation for K_2 , plus j and q) are listed in Table 2, and together with the coefficients for K_1 these represent the model solubility for saline fluids. We evaluated the quality of the model by comparison between calculated and experimentally determined solubility values over a wide range of pressure, temperature, and salinity, including against experimental data that were not used in the regression analysis (Zajacz et al. 2018, Scheuermann et al. 2019). We applied the model to assess the trends in solubility with variation in these same independent variables, and along model fluid flow pathways of various hydrothermal ore-forming system types.

3. Results

3.1 Solubility Model and Goodness of Fit

The solubility model was calibrated based on experimental data covering the ranges from 25 to 800 C, 0.1 to 1400 MPa, and 0 to 60 wt % NaCl. The coefficients are listed in Table 2. The “R-squared” values for each fitted equation were 0.98 for the K_1 expression and 0.86 for the K_2 expression.

Overall, the spread in absolute (Fig. 1A) and relative (Fig. 1B) residuals does not show a bias to more negative or positive values and the majority of calculated solubility values are within 50% relative error compared to their respective experimental values (Fig. 1b). The calculated solubilities from our model follow a clear 1:1 trend in comparison to their respective experimental values for all data sets (Fig. 2a). Experimental data from Scheuermann et al.

(2019), mostly for solubility of anhydrite in the vapor phases within the two-phase liquid+vapor field, were not used in calibrating our solubility model, and were used instead to evaluate the accuracy of the model after calibration. Comparing the experimental data points from Scheuermann et al. (2019) with the corresponding values calculated using our model reveals an approximately linear 1:1 trend, which further demonstrates that our solubility model works well for fluids of vapor-like density and at conditions outside the range of the data used in the calibration (Fig. 2b). Similarly, comparison with the recent experimental data from Zajacz et al. (2018), which were based on experiments at magmatic-hydrothermal conditions of 800 °C and 240 MPa and in saline brines up to >50 wt% NaCl, show a very good match between the calculated and experimentally derived values (Fig. 2c).

3.2 Effects of Pressure, Temperature, and Salinity

Our model allows us to explore how the solubility of anhydrite varies as function of temperature, pressure, and salinity. The modeled solubility curves presented in this section are calculated for conditions in which the fluid is a single phase, thus the solubility curves displayed in the figures are truncated by the intersections with phase boundaries, namely the liquid + vapor envelope and/or the liquid + halite liquidus surface. Scenarios of liquid-vapor immiscibility and their effect on solubility are modeled in the subsequent section. Pressure, temperature, and salinity all have a strong effect on the solubility of anhydrite, and the effects of these three variables are discussed below.

Solubility of anhydrite is positively correlated with pressure over the full range of conditions modeled here. At constant temperature and salinity, the solubility of anhydrite increases with increasing pressure (Fig. 4), and this positive correlation is amplified at higher

salinity (Fig. 4). This effect is also evident when comparing solubility as a function of either temperature (Fig. 3) or salinity (Fig. 5) at different constant pressures.

The effect of temperature on the solubility of anhydrite is more complex compared to that of pressure. At relatively low temperatures, the solubility of anhydrite shows retrograde temperature dependence hence, the solubility of anhydrite first decreases with increasing temperature (Fig. 3). However, at higher temperature conditions, the solubility of anhydrite transitions from retrograde to prograde temperature dependence (Fig 3, Fig 5), and hence the solubility of anhydrite increases with increasing temperature thereafter. The transition from retrograde to prograde temperature dependence gives rise to a local minimum of anhydrite solubility, manifested as “U-shaped” solubility-versus-temperature curves. The temperature at which the transition from retrograde to prograde solubility occurs shifts to lower values with increasing pressure, and to higher values with increasing salinity (Fig. 3). Moreover, the magnitude of the temperature dependence of solubility (both retrograde and prograde) increases with increasing salinity (Fig. 3).

Increasing fluid salinity strongly increases the solubility of anhydrite - i.e., anhydrite shows strong salting-in behaviour. This positive correlation is clear across all P-T-X scenarios modeled in this study (Fig. 3, Fig. 4, Fig. 5). The effect of salinity is arguably the most intense amongst the three variables (P, T, and X), in the sense that an increase in salinity from zero to 20 wt% NaCl raises solubility of anhydrite by a significantly wider margin than any change in temperature or pressure over the full range considered here.

The various trends/effect of pressure and temperature for a given salinity can all be captured simultaneously in solubility contour diagrams (Fig. 6). For all fluid salinities, the

solubility of anhydrite is highest at conditions of high pressure/low temperature and high pressure/high temperature (Fig. 6). The previously mentioned “U-shaped” solubility trends are clearly illustrated, where a local minimum of solubility exists between low and high pressure-temperature conditions, corresponding to the transition of anhydrite solubility from retrograde temperature dependence to prograde temperature dependence (Fig. 6). Again, fluid salinity exercises strong control on the solubility of anhydrite, with anhydrite solubility increasing by orders of magnitude towards higher salinities (Fig. 6d). The contour diagrams in pressure-temperature space are discussed further below in predicting the dissolution or precipitation of anhydrite along model fluid flow paths representative of various hydrothermal systems.

3.3. Solubility of Anhydrite under Conditions of Liquid-Vapor Immiscibility

Liquid-vapor phase separation is a common phenomenon in various hydrothermal settings (Steele-MacInnis et al. 2021) and has been previously shown to exert strong control on solubility, dissolution, and precipitation of quartz (Steele-MacInnis et al. 2012a, b; Monecke et al. 2018; 2019; Li et al. 2020). Similarly, Scheuermann et al. (2019) showed experimentally that the solubility of anhydrite is strongly influenced by liquid-vapor immiscibility. Indeed, a first-order prediction based on our present results that show a strong salting-in of anhydrite solubility is that liquid-vapor immiscibility of saline fluids (in which the vapor phase produced has a relatively low salinity, whereas the liquid phase produced is generally a highly saline brine) will exert an even stronger control on the solubility of anhydrite, compared to quartz. Three isobaric scenarios are presented here, in which a liquid with a salinity of 10 wt% NaCl experiences an increase in temperature until it intersects the boundary of the liquid + vapor envelope (Fig. 7). Within the liquid + vapor envelope, the initially single-phase fluid separates into a highly saline liquid and a low salinity vapor (Fig. 7). When this takes place at a pressure equal to that of the

critical point for a given salinity (i.e., at the critical pressure, or the intersection of the bubble-point and dew-point curves), the solubility lines for the brine and the vapor both originate smoothly from the critical point on the phase boundary without any step-change in solubility (Fig. 7B). As expected, the solubility of anhydrite is significantly higher in the high-salinity/high-density brine phase than in the low-salinity/low-density vapor phase, and solubility in the brine continues to increase with increasing temperature. When the same process of phase separation takes place at pressures below the critical point (i.e., along the bubble-point curve), the solubility line for the brine phase continues smoothly from the single-phase fluid, whereas there is an abrupt step in the solubility between the single-phase fluid and the vapor phase (Fig. 7A). Conversely, when this process of phase separation takes place at pressures above the critical point (i.e., along the dew-point curve), the vapor solubility line continues smoothly from that of the single-phase fluid and the brine solubility line is offset with a step-change to much higher solubility (Fig. 7C). These trends have strong implications for hydrothermal systems where boiling is common, as the aqueous brine phase has significantly more capacity than the vapor phase to transport calcium and sulfate.

4. Discussion

4.1. Major Controls on Anhydrite Solubility

The results of the solubility model reflect the fundamental speciation and solvation behavior of calcium and sulfate in aqueous solutions. Previous studies have indicated that the solubility behaviour of anhydrite is analogous to that of calcite (Newton and Manning 2002, 2005). Like calcite, anhydrite shows strong salting-in behavior, as well as retrograde solubility at low temperatures (Newton and Manning 2005). This similarity is also noticeable when

comparing the calculated coefficients for calcite from Brooks and Steele-MacInnis (2019) with that of the calculated coefficients in this study. Coefficients a through e for both K_1 and K_2 equations for calcite are of the same sign as the coefficients for anhydrite (Brooks and Steele-MacInnis 2019). The magnitudes of these coefficients are either within the same order of magnitude, or within one order of magnitude of each other. This implies that both calcite and anhydrite yield similar charged species in solution which interact strongly with H_2O (Dolejš and Manning 2010). Brooks and Steele-MacInnis stated that the best fit of the stoichiometric coefficients for calcite gave results of $j = 1$ and $q = 1$, which are the same values obtained in this study during model calibration for anhydrite. Scheuermann et al. (2019) investigated the speciation of dissolved anhydrite in low-density vapor, and concluded that species present included the neutral species Na_2SO_4 and $CaCl_2$, as well as the charged species $NaSO_4^-$, $CaCl^+$, Ca^{2+} , and $CaOH^+$. The derived stoichiometric coefficients of j and q can be used to estimate quantitatively a basic (overall) stoichiometry of the dissolution reaction, and thus outline a series of hypothetical reactions for anhydrite in aqueous solution (Eq. 2, 3). The stoichiometric coefficient of $j = 1$ could be represented by the hypothetical reaction $CaSO_4 + H_2O = CaOH^+ + HSO_4^-$ and the stoichiometric coefficient of $q = 1$ can be represented by the hypothetical reaction $CaOH^+ + HSO_4^- + NaCl = CaCl^+ + NaSO_4^- + H_2O$. Dolejš and Manning (2010) concluded that solvent density had a strong effect on the solubilities of Ca-bearing minerals (calcite, apatite, fluorite, and portlandite), and that the dissolution of these minerals tends to yield charged species. Our results suggest the same conclusion can be extended to anhydrite. The creation of charged species as a result of dissolution also promotes the hydration shell to experience electrostriction effects, which leads to increasingly negative partial molar volumes as the charge of the species increases (Dolejš and Manning 2010). This electrostriction in association with

charged species explains why increasing pressure leads to increased solubility of the Ca-bearing mineral (Dolejš and Manning 2010). This effect of pressure on solubility is also verified for anhydrite in this study. Our solubility model also shows that fluid salinity is a major control on the solubility of anhydrite, which is also observed in previous solubility research (Newton and Manning 2005). The role fluid salinity plays in anhydrite solubility is clear in scenarios of liquid-vapor immiscibility (Fig. 7). In these instances of boiling, the solubility of anhydrite in the brine phase is up to several orders or magnitude greater than in the vapor phase, suggesting that brines have the capacity to transport relatively large amounts of calcium and sulfate in solution during liquid + vapor coexistence.

4.2. Example Applications to Hydrothermal Ore-Forming Systems

4.2.1 Applications to VMS deposits and active sub-seafloor hydrothermal systems

At active sub-seafloor hydrothermal systems, which generate VMS deposits, the circulation and mixing of seawater with hydrothermal fluids within the ridge leads to abrupt temperature changes as well as boiling. A representative fluid flow path for such a system is shown in Fig. 8 (Steele-MacInnis et al. 2021), superimposed on solubility contours of anhydrite in pressure-temperature space. Points along the path have been indicated to guide the eye between the different panels of Fig. 8, and to highlight the changes in the solubility of anhydrite (as well as quartz, Brooks and Steele-MacInnis 2019) along the flow path (Fig. 8). As seawater is initially circulated at relatively low pressures down into the ridge and temperature increases from approximately 100°C to 350°C, the solubility of anhydrite decreases so there is potential for anhydrite precipitation to occur in the recharge regions of the system (Fig. 8). In contrast, solubility of quartz mostly *increases* during this same fluid influx into the hydrothermal system, and as such, anhydrite deposited in the recharge zone will generally be without coeval quartz.

The only exception to the latter is as the fluid is eventually above ~ 400 °C, where the solubility of quartz transitions to retrograde temperature dependence and quartz may be deposited along a heating path (Steele-MacInnis et al. 2012a, b). As the fluid temperature increases further, the liquid + vapor phase boundary envelope is intersected conditions close to the critical point for this fluid, and phase separation occurs (point C, Fig. 8). Under these conditions of liquid + vapor coexistence, we model both the solubility of anhydrite and quartz in the high salinity liquid phase, the low salinity vapor phase, as well as a mass-balanced bulk solubility in the two-phase mixture (with bulk salinity held constant) (Fig. 8B). Both the solubility of anhydrite in the brine phase and the bulk mixture significantly increase compare to the initial single phase liquid (Fig. 8B), suggesting that anhydrite will generally not be deposited at this stage, or will even (re-)dissolve if present in the rock. In contrast, quartz solubility in the bulk mixture decreases substantially throughout this temperature range (Fig. 8C), leading to quartz deposition in the boiling zone (Steele-MacInnis et al. 2012a, b). This divergent behavior of quartz versus anhydrite mainly reflects the very strong salting-in of anhydrite, which serves to keep the bulk solubility relatively high as the fluid boils. However, as the fluid ascends and cools the solubility of anhydrite in the brine begins to decrease (Fig. 8B) and some anhydrite may be deposited at the top of the boiling zone. Thereafter, as the single-phase fluid ascends towards the seafloor vent, quartz is deposited throughout whereas anhydrite is not predicted, except where ascending hydrothermal fluid mixes with cold seawater (Pujatti et al. 2021).

4.2.2 Applications to Porphyry copper deposits

Anhydrite is a common gangue mineral in porphyry-Cu deposits, occurring both as an igneous mineral in the causative plutonic rocks (Hutchison and Dilles 2019), as a vein-forming mineral, and as a common mineral inclusion enclosed within hydrothermal quartz (Steele-

MacInnis et al. 2021). As deep fluids are exsolved from the pluton, the decreasing pressure-temperature conditions initially promote a decrease in the solubilities of both anhydrite and quartz in the fluid, and hence the precipitation of high-temperature quartz + anhydrite veins is predicted to occur (point A to B, Fig. 9). In the two-phase liquid + vapor region, the solubility of anhydrite in the fluid first increases by several orders of magnitude, hence this fluid may have the potential to dissolve anhydrite existing in wall rock or previously deposited in fractures/veins (point B to C, Fig. 9). Over this same temperature range, the solubility of quartz in the boiling fluid decreases monotonically and hence quartz veins lacking anhydrite are expected to form along this part of the flow path (point b to C, Fig. 9). Similarly to model predictions in VMS analogous systems, as the hydrothermal fluid reaches the low-T region of the system, transitioning from the two-phase liquid + vapor region back to the single phase, the solubility of anhydrite in the fluid drastically decreases (point C to D, Fig. 9). This major decrease likely promotes deposition of anhydrite where ore mineralization occurs in the system, which is supported by field observations of anhydrite. Importantly, this same portion of the flow path (point C to D, Fig. 9) corresponds to a region where quartz deposition is not expected (owing to the retrograde temperature dependence of quartz solubility in this region, Monecke et al. 2018), and ore mineralization is expected to occur as a result of the substantial temperature dependence of chalcopyrite solubility (Steele-MacInnis et al. 2021). Hence, our results suggest that anhydrite deposition may be closely associated with ore mineralization in veins that lack quartz (point D, Fig. 9, Monecke et al. 2018).

5. Conclusions

Our thermodynamic model for the solubility of anhydrite in H₂O-NaCl fluids is applicable to a broad range of crustal settings, and is calibrated for conditions of 25 to 800 °C, 0.1 to 1400 MPa, and 0 to 60 wt% NaCl. In addition to reproducing experimental data trends within error, our solubility model is also shown to be capable of yielding accurate results for conditions outside of the experimental dataset used in calibration. Modeling the solubility of anhydrite at various P-T-X conditions shows that fluid salinity has the strongest control on the solubility of anhydrite compared to changes in pressure and temperature. This strong salting-in behaviour of anhydrite is also clear in modeled scenarios of liquid + vapor immiscibility, where the solubility of anhydrite significantly increases in the high-density/high-salinity brine phase during boiling. With our solubility model, it is now possible to quantitatively predict the potential precipitation and/or dissolution of anhydrite in hydrothermal ore-forming systems during fluid evolution.

References

- Akinfiyev, N. N., & Diamond, L. W. (2009). A simple predictive model of quartz solubility in water-salt-CO₂ systems at temperatures up to 1000 °C and pressures up to 1000 MPa. *Geochimica et Cosmochimica Acta*, 73(6), 1597–1608. <https://doi.org/10.1016/j.gca.2008.12.011>
- Bain, W. M., Steele-MacInnis, M., Li, K., Li, L., Mazdab, F. K., & Marsh, E. E. (2020). A fundamental role of carbonate–sulfate melts in the formation of iron oxide–apatite deposits. *Nature Geoscience*, 13(11), 751–757. <https://doi.org/10.1038/s41561-020-0635-9>
- Bain, W. M., Steele-MacInnis, M., Tornos, F., Hanchar, J. M., Creaser, E. C., & Pietruszka, D. K. (2021). Evidence for iron-rich sulfate melt during magnetite(-apatite) mineralization at El Laco, Chile. *Geology*, 49 (9): 1044–1048. <https://doi.org/10.1130/g48861.1>
- Block, J., & Waters, O. B. (1968). The NaCl-Na₂SO₄-CaSO₄-H₂O system at 25 °C to 100 °C. *J. Chem. Eng. Data*, 13, 336–344.
- Blount, C. W., & Dickson, F. W. (1969). The solubility of anhydrite (CaSO₄) in NaCl-H₂O from 100 to 450°C and 1 to 1000 bars. *Geochimica et Cosmochimica Acta*, 33(2), 227–245. [https://doi.org/10.1016/0016-7037\(69\)90140-9](https://doi.org/10.1016/0016-7037(69)90140-9)
- Blundy, J., Mavrogenes, J., Tattitch, B., Sparks, S., & Gilmer, A. (2015). Generation of porphyry copper deposits by gas-brine reaction in volcanic arcs. *Nature Geoscience*, 8(3), 235–240. <https://doi.org/10.1038/ngeo2351>
- Bock, E. (1961). On the solubility of anhydrous calcium sulphate and of gypsum in concentrated solutions of sodium chloride. *Canadian Journal of Chemistry*, 39(1061), 1746–1751.
- Broman, C., Nyström, J. O., Henríquez, F., & Elfman, M. (1999). Fluid inclusions in magnetite-apatite ore from a cooling magmatic system at El Laco, Chile. *GFF*, 121(3), 253–267. <https://doi.org/10.1080/11035899901213253>
- Brooks, H. L., & Steele-MacInnis, M. (2019). A model for the solubility of minerals in saline aqueous fluids in the crust and upper mantle. *American Journal of Science*, 319(9), 754–787. <https://doi.org/10.2475/09.2019.02>
- Cline, J. S., Bodnar, R. J., & Rimstidt, J. D. (1992). Numerical simulation of fluid flow and silica transport and deposition in boiling hydrothermal solutions: Application to epithermal gold deposits. *Journal of Geophysical Research: Solid Earth*, 97(B6), 9085–9103. <https://doi.org/https://doi.org/10.1029/91JB03129>
- Cooke, D. R., Hollings, P., Wilkinson, J. J., & Tosdal, R. M. (2014). Geochemistry of Porphyry Deposits. In *Treatise on Geochemistry: Second Edition* (2nd ed., Vol. 13). <https://doi.org/10.1016/B978-0-08-095975-7.01116-5>

- Cui, H., Zhong, R., Xie, Y., Yuan, X., Liu, W., Brugger, J., & Yu, C. (2020). Forming sulfate- and REE-rich fluids in the presence of quartz. *Geology*, *48*(2), 145–148. <https://doi.org/10.1130/G46893.1>
- Dolejš, D., & Manning, C. E. (2010). Thermodynamic model for mineral solubility in aqueous fluids: Theory, calibration and application to model fluid-flow systems. *Geofluids*, *10*(1–2), 20–40. <https://doi.org/10.1111/j.1468-8123.2010.00282.x>
- Dolejš, D. (2013). Thermodynamics of Aqueous Species at High Temperatures and Pressures: Equations of State and Transport Theory. *Reviews in Mineralogy and Geochemistry*, *76*(1), 35–79. <https://doi.org/10.2138/rmg.2013.76.3>
- Driesner, T. (2007). The system H₂O-NaCl. Part II: Correlations for molar volume, enthalpy, and isobaric heat capacity from 0 to 1000 °C, 1 to 5000 bar, and 0 to 1 XNaCl. *Geochimica et Cosmochimica Acta*, *71*(20), 4902–4919. <https://doi.org/10.1016/j.gca.2007.05.026>
- Driesner, T., & Heinrich, C. A. (2007). The system H₂O-NaCl. Part I: Correlation formulae for phase relations in temperature-pressure-composition space from 0 to 1000 °C, 0 to 5000 bar, and 0 to 1 XNaCl. *Geochimica et Cosmochimica Acta*, *71*(20), 4880–4901. <https://doi.org/10.1016/j.gca.2006.01.033>
- Fournier, R. O. (1983). A method of calculating quartz solubilities in aqueous sodium chloride solutions. *Geochimica et Cosmochimica Acta*, *47*(3), 579–586. [https://doi.org/https://doi.org/10.1016/0016-7037\(83\)90279-X](https://doi.org/https://doi.org/10.1016/0016-7037(83)90279-X)
- Fournier, R. O., & Potter, R. W. (1982). An equation correlating the solubility of quartz in water from 25° to 900°C at pressures up to 10,000 bars. *Geochimica et Cosmochimica Acta*, *46*(10), 1969–1973. [https://doi.org/https://doi.org/10.1016/0016-7037\(82\)90135-1](https://doi.org/https://doi.org/10.1016/0016-7037(82)90135-1)
- Fouquet, Y., Henry, K., Knott, R., & Cambon, P. (1998). Geochemical section of the TAG hydrothermal mound. *Proceedings of the Ocean Drilling Program: Scientific Results*, *158*(February), 363–387. <https://doi.org/10.2973/odp.proc.sr.158.216.1998>
- Glew, D. N., & Hames, D. A. (1970). Gypsum, disodium pentacalcium sulfate, and anhydrite solubilities in concentrated sodium chloride solutions. *Canadian Journal of Chemistry*, *48*(23), 3733–3738. <https://doi.org/10.1139/v70-623>
- Hedenquist, J. W., Arribas, A. R., & Aoki, M. (2017). Zonation of sulfate and sulfide minerals and isotopic composition in the Far Southeast Porphyry and Lepanto Epithermal Cu–Au Deposits, Philippines. *Resource Geology*, *67*, 174–196. <https://doi.org/10.1111/rge.12127>
- Heinrich, C. A., Driesner, T., Stefánsson, A., & Seward, T. M. (2004). Magmatic vapor contraction and the transport of gold from the porphyry environment to epithermal ore deposits. *Geology*, *32*(9), 761–764. <https://doi.org/10.1130/G20629.1>

- Helgeson, H. C., & Kirkham, D. H. (1976). Theoretical prediction of the thermodynamic properties of aqueous electrolytes at high pressures and temperatures. III. Equation of state for aqueous species at infinite dilution. *American Journal of Science*, 276(2), 97 LP – 240. <https://doi.org/10.2475/ajs.276.2.97>
- Helgeson, H. C., Kirkham, D. H., & Flowers, G. C. (1981). Theoretical prediction of the thermodynamic behavior of aqueous electrolytes by high pressures and temperatures; IV, Calculation of activity coefficients, osmotic coefficients, and apparent molal and standard and relative partial molal properties to 600 d. *American Journal of Science*, 281(10), 1249 LP – 1516. <https://doi.org/10.2475/ajs.281.10.1249>
- Holland, H. D. (2005). Sedimentary mineral deposits and the evolution of Earth's near-surface environments. *Economic Geology*, 100(8), 1489–1509. <https://doi.org/10.2113/gsecongeo.100.8.1489>
- Hutchinson, M. C., & Dilles, J. H. (2019). Evidence for magmatic anhydrite in porphyry copper intrusions. *Economic Geology*, 114(1), 143–152. <https://doi.org/10.5382/econgeo.2019.4624>
- Hutchinson, M. C., Brooker, R. A., Dilles, J. H., & Blundy, J. (2020). The stability and composition of sulfate melts in arc magmas. *Contributions to Mineralogy and Petrology*, 175(10), 92. <https://doi.org/10.1007/s00410-020-01729-6>
- James, R. H., Green, D. R. H., Stock, M. J., Alker, B. J., Banerjee, N. R., Cole, C., German, Huvenne, V. A. I., Powell, A. M., C. R., Connelly, D. P. (2014). Composition of hydrothermal fluids and mineralogy of associated chimney material on the East Scotia Ridge back-arc spreading centre. *Geochimica et Cosmochimica Acta*, 139, 47–71. <https://doi.org/10.1016/j.gca.2014.04.024>
- Johnson, J. W., Oelkers, E. H., & Helgeson, H. C. (1992). SUPCRT92: A software package for calculating the standard molal thermodynamic properties of minerals, gases, aqueous species, and reactions from 1 to 5000 bar and 0 to 1000°C. *Computers & Geosciences*, 18(7), 899–947. [https://doi.org/https://doi.org/10.1016/0098-3004\(92\)90029-Q](https://doi.org/https://doi.org/10.1016/0098-3004(92)90029-Q)
- Klyukin, Y. I., Haroldson, E. L., & Steele-MacInnis, M. (2020). A comprehensive numerical model for the thermodynamic and transport properties of H₂O-NaCl fluids. *Chemical Geology*, 557(June). <https://doi.org/10.1016/j.chemgeo.2020.119840>
- Leach, D. L., Sangster, D. F., Kelley, K. D., Large, R. R., Garven, G., Allen, C. R., Gutzmer, J., & Walters, S. (2005). Sediment-hosted lead-zinc deposits: A global perspective. *Economic Geology*, 100, 561-607. <https://doi.org/10.5382/AV100.18>
- Li, X. H., Klyukin, Y. I., Steele-MacInnis, M., Fan, H. R., Yang, K. F., & Zoheir, B. (2020). Phase equilibria, thermodynamic properties, and solubility of quartz in saline-aqueous-carbonic fluids: Application to orogenic and intrusion-related gold deposits. *Geochimica et Cosmochimica Acta*, 283, 201–221. <https://doi.org/10.1016/j.gca.2020.06.008>

- Lowell, R. P., Yao, Y., & Germanovich, L. N. (2003). Anhydrite precipitation and the relationship between focused and diffuse flow in seafloor hydrothermal systems. *Journal of Geophysical Research: Solid Earth*, 108(B9), 1–8. <https://doi.org/10.1029/2002jb002371>
- Madgin, W. M., & Swales, D. A. (1956). Solubilities in the system CaSO₄-NaCl-H₂O at 25° and 35°. *Journal of Applied Chemistry*, 6(11), 482–487. <https://doi.org/10.1002/jctb.5010061102>
- Manning, C. E. (1994). The solubility of quartz in H₂O in the lower crust and upper mantle. *Geochimica et Cosmochimica Acta*, 58(22), 4831–4839. [https://doi.org/10.1016/0016-7037\(94\)90214-3](https://doi.org/10.1016/0016-7037(94)90214-3)
- Marshall, W. L., & Quist, A. S. (1967). A representation of isothermal ion-ion-pair solvent equilibria independent of changes in dielectric constant. *Proceedings of the National Academy of Science*, 58, 901–906. <https://doi.org/10.1073/pnas.58.3.901>
- Marshall, W. L., Slusher, R., & Jones, E. V. (1964). Aqueous Systems at High Temperatures XIV. Solubility and Thermodynamic Relationships for CaSO₄ in NaCl-H₂O Solutions from 40 to 200 °C., 0 to 4 Molal NaCl. *Journal of Chemical & Engineering Data*, 9(2), 187–191. <https://doi.org/10.1021/jc60021a011>
- Monecke, T., Monecke, J., James Reynolds, T., Tsuruoka, S., Bennett, M. M., Skewes, W. B., & Palin, R. M. (2018). Quartz solubility in the H₂O-NaCl system: A framework for understanding vein formation in porphyry copper deposits. *Economic Geology*, 113(5), 1007–1046. <https://doi.org/10.5382/ECONGEO.2018.4580>
- Monecke, T., Monecke, J., & Reynolds, T. J. (2019). The influence of CO₂ on the solubility of quartz in single-phase hydrothermal fluids: Implications for the formation of stockwork veins in porphyry copper deposits. *Economic Geology*, 114(6), 1195–1206. <https://doi.org/10.5382/econgeo.4680>
- Nehlig, P. (1991). Salinity of oceanic hydrothermal fluids: a fluid inclusion study. *Earth and Planetary Science Letters*, 102(3–4), 310–325. [https://doi.org/10.1016/0012-821X\(91\)90026-E](https://doi.org/10.1016/0012-821X(91)90026-E)
- Newton, R. C., & Manning, C. E. (2002). Experimental determination of calcite solubility in H₂O-NaCl solutions at deep crust/upper mantle pressures and temperatures: Implications for metasomatic processes in shear zones. *American Mineralogist*, 87(10), 1401–1409. <https://doi.org/10.2138/am-2002-1016>
- Newton, R. C., & Manning, C. E. (2005). Solubility of anhydrite, CaSO₄, in NaCl-H₂O solutions at high pressures and temperatures: Applications to fluid-rock interaction. *Journal of Petrology*, 46(4), 701–716. <https://doi.org/10.1093/petrology/egh094>
- Ohmoto, H. (1972). Systematics of Sulfur and Carbon Isotopes in Hydrothermal Ore Deposits. *Economic Geology*, 67(5), 551–578. <https://doi.org/10.2113/gsecongeo.67.5.551>

- Oppenheimer, C., Scaillet, B., & Martin, R. S. (2011). Sulfur degassing from volcanoes: Source conditions, surveillance, plume chemistry and earth system impacts. *Reviews in Mineralogy and Geochemistry*, 73, 363–421. <https://doi.org/10.2138/rmg.2011.73.13>
- Orovan, E. A., Cooke, D. R., Harris, A. C., Ackerman, B., & Lawlis, E. (2018). Geology and isotope geochemistry of the Wainaulo Cu-Au porphyry deposit, Namosi District, Fiji. *Economic Geology*, 113(1), 133–161. <https://doi.org/10.5382/econgeo.2018.4546>
- Petersen, S., Herzig, P. M., & Hannington, M. D. (2000). Third dimension of a presently forming VMS deposit: TAG hydrothermal mound, Mid-Atlantic Ridge, 26°N. *Mineralium Deposita*, 35(2), 233–259. <https://doi.org/10.1007/s001260050018>
- Pokrovski, G. S., Borisova, A. Y., & Harrichoury, J. C. (2008). The effect of sulfur on vapor-liquid fractionation of metals in hydrothermal systems. *Earth and Planetary Science Letters*, 266(3–4), 345–362. <https://doi.org/10.1016/j.epsl.2007.11.023>
- Pujatti, S., Klyukin, Y., Steele-MacInnis, M., & Tutolo, B. M. (2021). Anhydrite replacement reaction in nodular pyrite breccia and its geochemical controls on the $\delta^{34}\text{S}$ signature of pyrite in the TAG hydrothermal mound, 26° N Mid Atlantic Ridge. *Lithos*, 400–401, 106357. <https://doi.org/https://doi.org/10.1016/j.lithos.2021.106357>
- Rye, R. O., Bethke, P. M., & Wasserman, M. D. (1992). The stable isotope geochemistry of acid sulfate alteration. *Economic Geology*, 87, 225–262. <https://doi.org/10.2113/gsecongeo.87.2.225>
- Scheuermann, P. P., Tutolo, B. M., & Seyfried, W. E. (2019). Anhydrite solubility in low-density hydrothermal fluids: Experimental measurements and thermodynamic calculations. *Chemical Geology*, 524(June), 184–195. <https://doi.org/10.1016/j.chemgeo.2019.06.018>
- Seward, T. M., Williams-Jones, A. E., & Migdisov, A. A. (2014). The chemistry of metal transport and deposition by ore-forming hydrothermal fluids. In *Treatise on Geochemistry: Second Edition* (2nd ed., Vol. 13). <https://doi.org/10.1016/B978-0-08-095975-7.01102-5>
- Shirey, S. B., Kamber, B. S., Whitehouse, M. J., Mueller, P. A., & Basu, A. R. (2008). A review of the isotopic and trace element evidence for mantle and crustal processes in the Hadean and Archean: Implications for the onset of plate tectonic subduction. *Special Paper of the Geological Society of America*, 440(01), 1–29. [https://doi.org/10.1130/2008.2440\(01\)](https://doi.org/10.1130/2008.2440(01))
- Sillitoe, R. H. (2010). Porphyry copper systems. *Economic Geology*, 105(1), 3–41. <https://doi.org/10.2113/gsecongeo.105.1.3>
- Steele-MacInnis, M., Han, L., Lowell, O. P., Rimstidt, J. D., & Bodnar, R. J. (2012). Quartz precipitation and fluid inclusion characteristics in sub-seafloor hydrothermal systems associated with volcanogenic massive sulfide deposits. *Central European Journal of Geosciences*, 4(2), 275–286. <https://doi.org/10.2478/s13533-011-0053-z>

- Steele-MacInnis, M., Han, L., Lowell, R. P., Rimstidt, J. D., & Bodnar, R. J. (2012). The role of fluid phase immiscibility in quartz dissolution and precipitation in sub-seafloor hydrothermal systems. *Earth and Planetary Science Letters*, 321–322, 139–151. <https://doi.org/10.1016/j.epsl.2011.12.037>
- Steele-MacInnis, M., Lecumberri-Sanchez, P., Marshall, D., & Kontak, D. J. (2021). Contributions of fluid inclusions to genetic models for mineral deposits. In P. Lecumberri-Sanchez, M. Steele-MacInnis, & D. J. Kontak (Eds.), *Fluid and Melt Inclusions: Applications to Geologic Processes* (Topics in Mineral Science Volume 49, pp. 195–242). Mineralogical Society of Canada.
- Sykora, S., Selley, D., Cooke, D. R., & Harris, A. C. (2018) The structure and significance of anhydrite-bearing vein arrays, Lienetz orebody, Lihir gold deposit, Papua New Guinea. *Economic Geology*, 113, 237-270. <https://doi.org/10.5382/econgeo.2018.4550>
- Szmihelsky, M., Steele-MacInnis, M., Bain, W.M., Falck, H., Adair, R., Campbell, B., Dufrane, S.A., Went, A., & Corlett, H.J. (2020). Mixing brine with oil triggered sphalerite deposition at Pine Point, Northwest Territories, Canada. *Geology*, 49(5), 488–492. <https://doi.org/10.1130/G48259.1>
- Sun, M., Monecke, T., Reynolds, T. J., & Yang, Z. (2021). Understanding the evolution of magmatic-hydrothermal systems based on microtextural relationships, fluid inclusion petrography, and quartz solubility constraints: insights into the formation of the Yulong Cu-Mo porphyry deposit, eastern Tibetan Plateau, C. *Mineralium Deposita*, 56(5), 823–842. <https://doi.org/10.1007/s00126-020-01003-6>
- Tanger, J. C., & Helgeson, H. C. (1988). Calculation of the thermodynamic and transport properties of aqueous species at high pressures and temperatures; revised equations of state for the standard partial molal properties of ions and electrolytes. *American Journal of Science*, 288(1), 19 LP – 98. <https://doi.org/10.2475/ajs.288.1.19>
- Templeton, C. C., & Rodgers, J. C. (1967). Solubility of anhydrite in several aqueous salt solutions between 250° and 325°C. *Journal of Chemical and Engineering Data*, 12(4), 536–547. <https://doi.org/10.1021/jc60035a020>
- Tivey, M. K., Humphris, S. E., Thompson, G., Hannington, M. D., & Rona, P. A. (1995). Deducing patterns of fluid flow and mixing within the TAG active hydrothermal mound using mineralogical and geochemical data. *Journal of Geophysical Research*, 100(B7). <https://doi.org/10.1029/95jb00610>
- Tornos, F., Velasco, F., & Hanchar, J. M. (2016). Iron-rich melts, magmatic magnetite, and superheated hydrothermal systems: The El Laco deposit, Chile. *Geology*, 44(6), 427–430. <https://doi.org/10.1130/G37705.1>

- Tornos, F., Velasco, F., & Hanchar, J. M. (2017). The magmatic to magmatic-hydrothermal evolution of the El Laco Deposit (Chile) and its implications for the genesis of magnetite-apatite deposits. *Economic Geology*, *112*(7), 1595–1628. <https://doi.org/10.5382/econgeo.2017.4523>
- Wagner, W., & Pruß, A. (2002). The IAPWS Formulation 1995 for the Thermodynamic Properties of Ordinary Water Substance for General and Scientific Use. *Journal of Physical and Chemical Reference Data*, *31*(2), 387–535. <https://doi.org/10.1063/1.1461829>
- Walter, B. F., Steele-MacInnis, M., & Markl, G. (2017). Sulfate brines in fluid inclusions of hydrothermal veins: Compositional determinations in the system H₂O-Na-Ca-Cl-SO₄. *Geochimica et Cosmochimica Acta*, *209*, 184–203. <https://doi.org/10.1016/j.gca.2017.04.027>
- Walter, B. F., Burisch, M., Fusswinkel, T., Marks, M. A. W., Steele-MacInnis, M., Wälle, M., Apukhtina, O. B., Markl, G. (2018). Multi-reservoir fluid mixing processes in rift-related hydrothermal veins, Schwarzwald, SW-Germany. *Journal of Geochemical Exploration*, *186*(October 2017), 158–186. <https://doi.org/10.1016/j.gexplo.2017.12.004>
- Walter, B. F., Steele-MacInnis, M., Giebel, R. J., Marks, M. A. W., & Markl, G. (2020). Complex carbonate-sulfate brines in fluid inclusions from carbonatites: Estimating compositions in the system H₂O-Na-K-CO₃-SO₄-Cl. *Geochimica et Cosmochimica Acta*, *277*, 224–242. <https://doi.org/10.1016/j.gca.2020.03.030>
- Walter, B. F., Giebel, R. J., Steele-MacInnis, M., Marks, M. A. W., Kolb, J., & Markl, G. (2021). Fluids associated with carbonatitic magmatism: A critical review and implications for carbonatite magma ascent. *Earth-Science Reviews*, *215*, 103509. <https://doi.org/10.1016/j.earscirev.2021.103509>
- Williams-Jones, A. E., & Heinrich, C. A. (2005). 100th Anniversary Special Paper: Vapor transport of metals and the formation of magmatic-hydrothermal ore deposits. *Economic Geology*, *100*(7), 1287–1312. <https://doi.org/10.2113/gsecongeo.100.7.1287>
- Zajacz, Z., Seo, J. H., Candela, P. A., Piccoli, P. M., Heinrich, C. A., & Guillong, M. (2010). Alkali metals control the release of gold from volatile-rich magmas. *Earth and Planetary Science Letters*, *297*(1–2), 50–56. <https://doi.org/10.1016/j.epsl.2010.06.002>
- Zajacz, Z., Candela, P. A., & Piccoli, P. M. (2017). The partitioning of Cu, Au and Mo between liquid and vapor at magmatic temperatures and its implications for the genesis of magmatic-hydrothermal ore deposits. *Geochimica et Cosmochimica Acta*, *207*, 81–101. <https://doi.org/10.1016/j.gca.2017.03.015>
- Zajacz, Z., Tsay, A., & Ghazali, N. (2018). The fate of sulfur at the magmatic-hydrothermal transition in the porphyry ore-forming environment. XIVth Pan-American Current Research on Fluid Inclusions (PACROFI-14), Abstracts with Program. June 12-14, Houston TX, USA.

Tables

Table 1: Summary of the experimental dataset on anhydrite solubility, and the respective ranges of pressure (P), temperature (T), and fluid salinity covered.

Reference	P (MPa)	T (°C)	Salinity (wt %)
Newton & Manning 2005	600 - 1400	600 - 800	0 - 58
Glew & Hames 1970	0.1	65	15 - 26
Blount & Dickson 1969	v.p - 100	100 - 450	0 - 29
Block & Waters 1968	0.1	85 - 100	0 - 19
Templeton & Rodgers 1967	v.p	250 - 325	0.001 - 25
Marshall et al. 1964	v.p	125 - 200	0.002 - 20
Bock 1961	0.1	25 - 50	0 - 27
Madgin & Swales 1956	0.1	25	0 - 26
Scheuermann et al. 2019 †	26.5 - 49.4	410 - 450	0.01 - 5
Zajacz et al. 2018	240	800	0 - 50

* v.p = vapor pressure

† not included in the regression analysis

Table 2: Coefficients of the solubility model.

	a (J mol ⁻¹)	b (J mol ⁻¹ K ⁻¹)	c (J mol ⁻¹ K ⁻¹)	d (J mol ⁻¹ K ⁻¹)	e (J mol ⁻¹ K ⁻¹)	j	q
K_1	38849.15	-1307.97	226.63	-0.2726	-131.318	-	-
K_2	4985.14	-8.8072	-	-	110.103	1	1

Figures

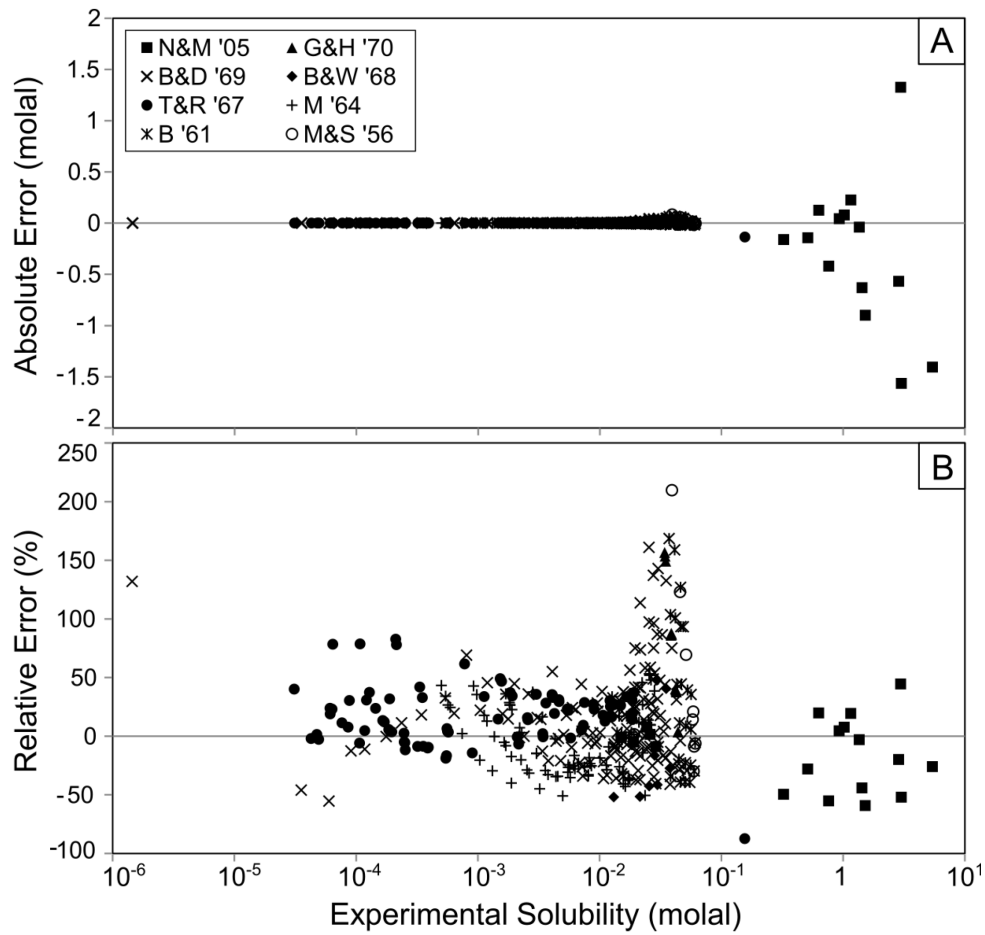


Figure 1. A: Absolute error (molal) versus experimental solubility (molal). B: Relative error versus experimental solubility (molal). References: N&M = Newton and Manning (2005), G&H = Glew and Hames (1970), B&D = Blount and Dickson (1969), B&W = Block and Waters (1968), T&R = Templeton and Rodgers (1967), M = Marshall et al. (1964), B = Bock (1961), M&S = Madgin and Swales (1956).

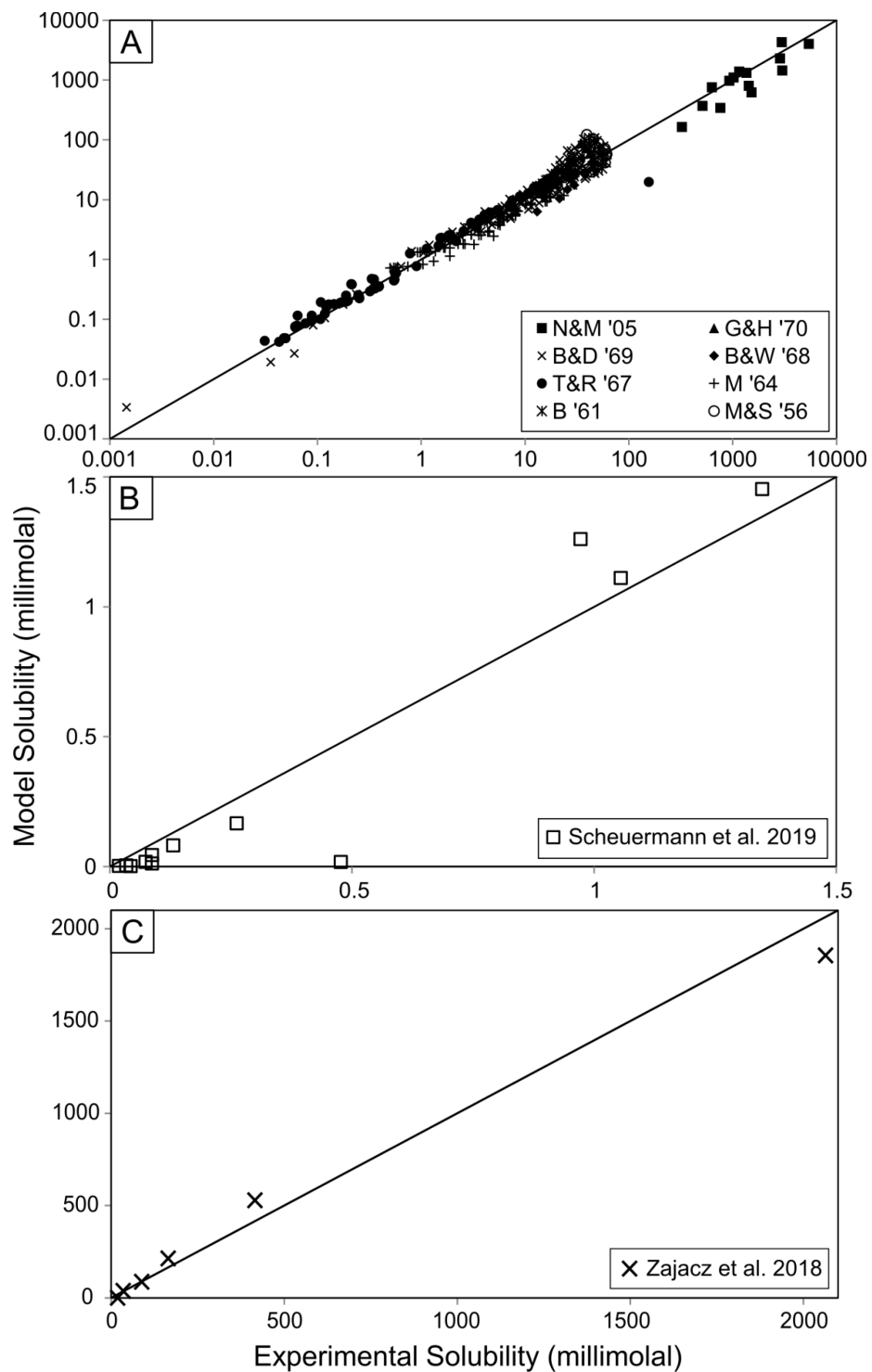


Figure 2. A: Model solubility (millimolal) versus experimental solubility (millimolal). References: N&M = Newton and Manning (2005), G&H = Glew and Hames (1970), B&D = Blount and Dickson (1969), B&W = Block and Waters (1968), T&R = Templeton and Rodgers (1967), M = Marshall et al. (1964), B = Bock (1961), M&S = Madgin and Swales (1956). B: Model solubility (millimolal) versus experimental solubility (millimolal) from Scheuermann et al. 2019. C: Model solubility (millimolal) versus experimental solubility (millimolal) from Zajacz et al. 2018.

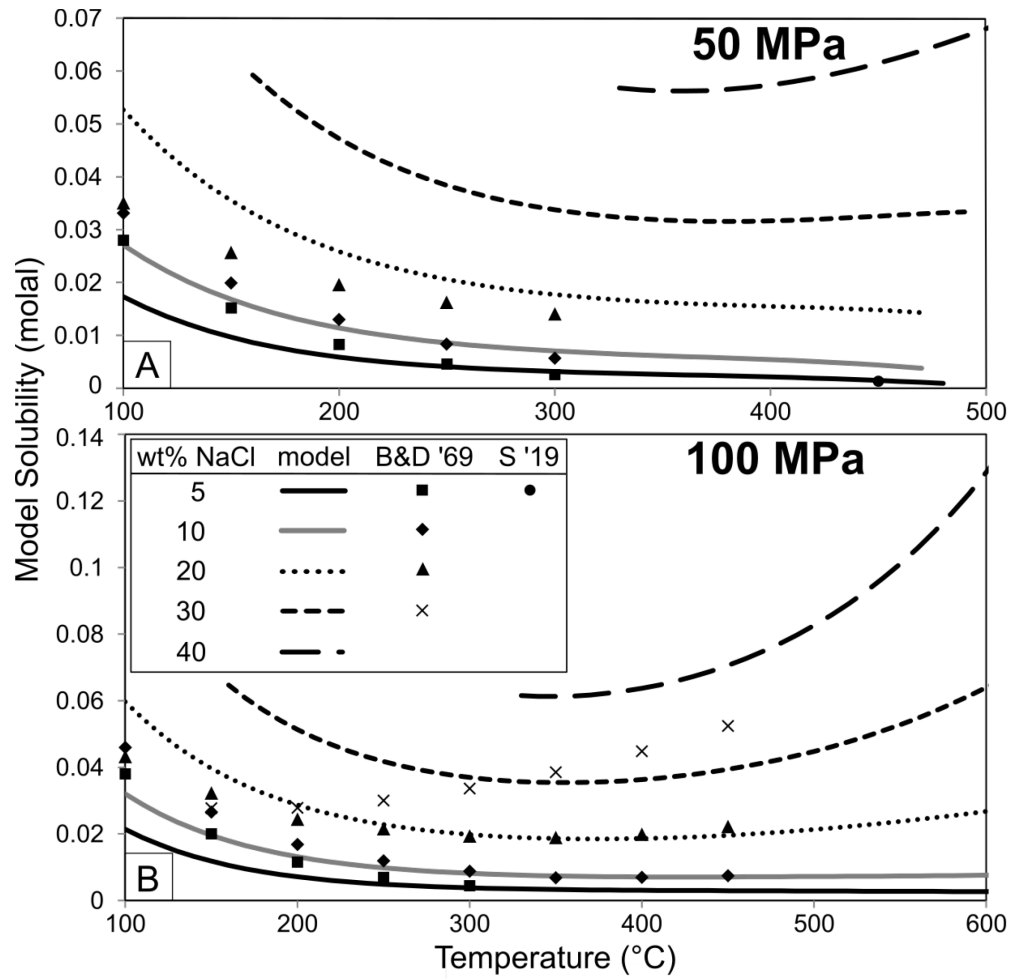


Figure 3. A: Model solubility of anhydrite (molal) versus temperature at 50 MPa. B: Model solubility of anhydrite (molal) versus temperature at 100 MPa. References: B&D = Blount and Dickson (1969), S = Scheuermann et al. (2019).

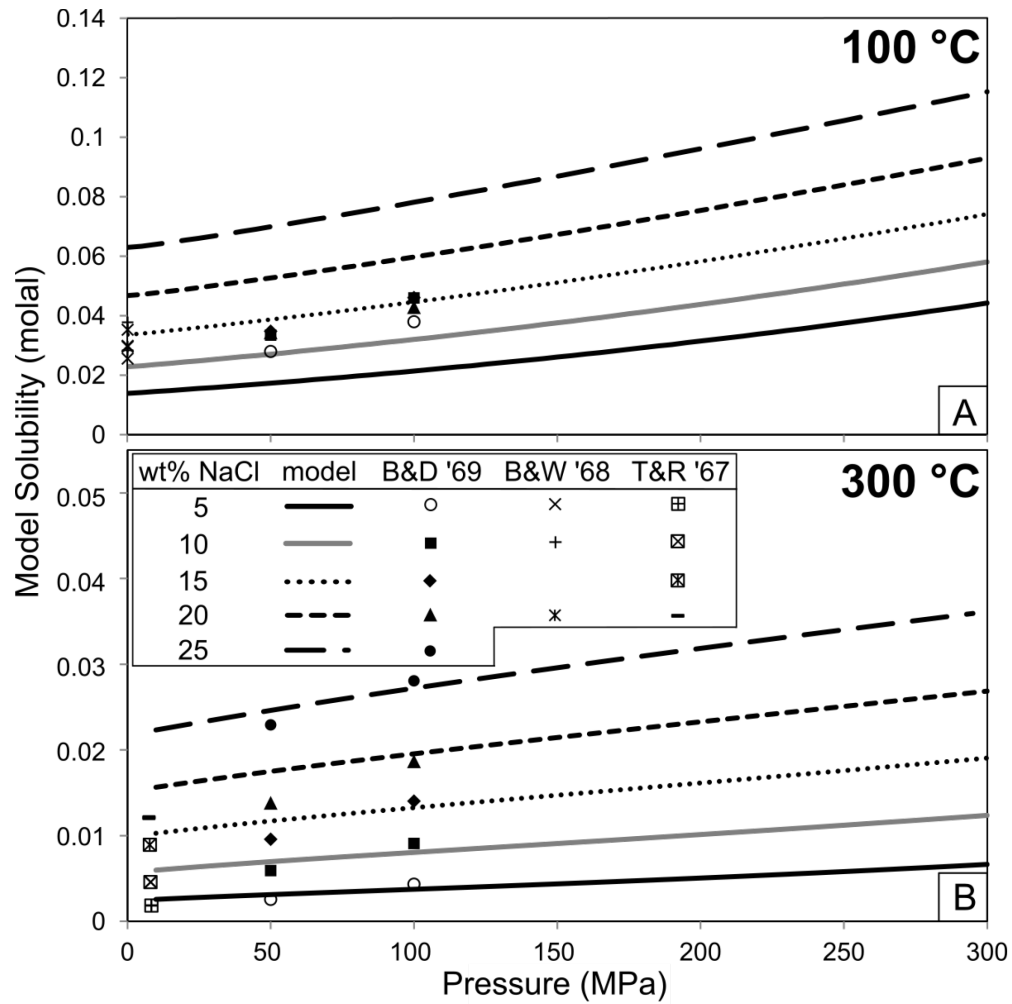


Figure 4. A: Model solubility of anhydrite (molal) versus pressure (bar) at 300 °C. B: Model solubility of anhydrite (molal) versus pressure (bar) at 100 °C. References: B&D = Blount and Dickson (1969), B&W = Block and Waters (1968), T&R = Templeton and Rodgers (1967).

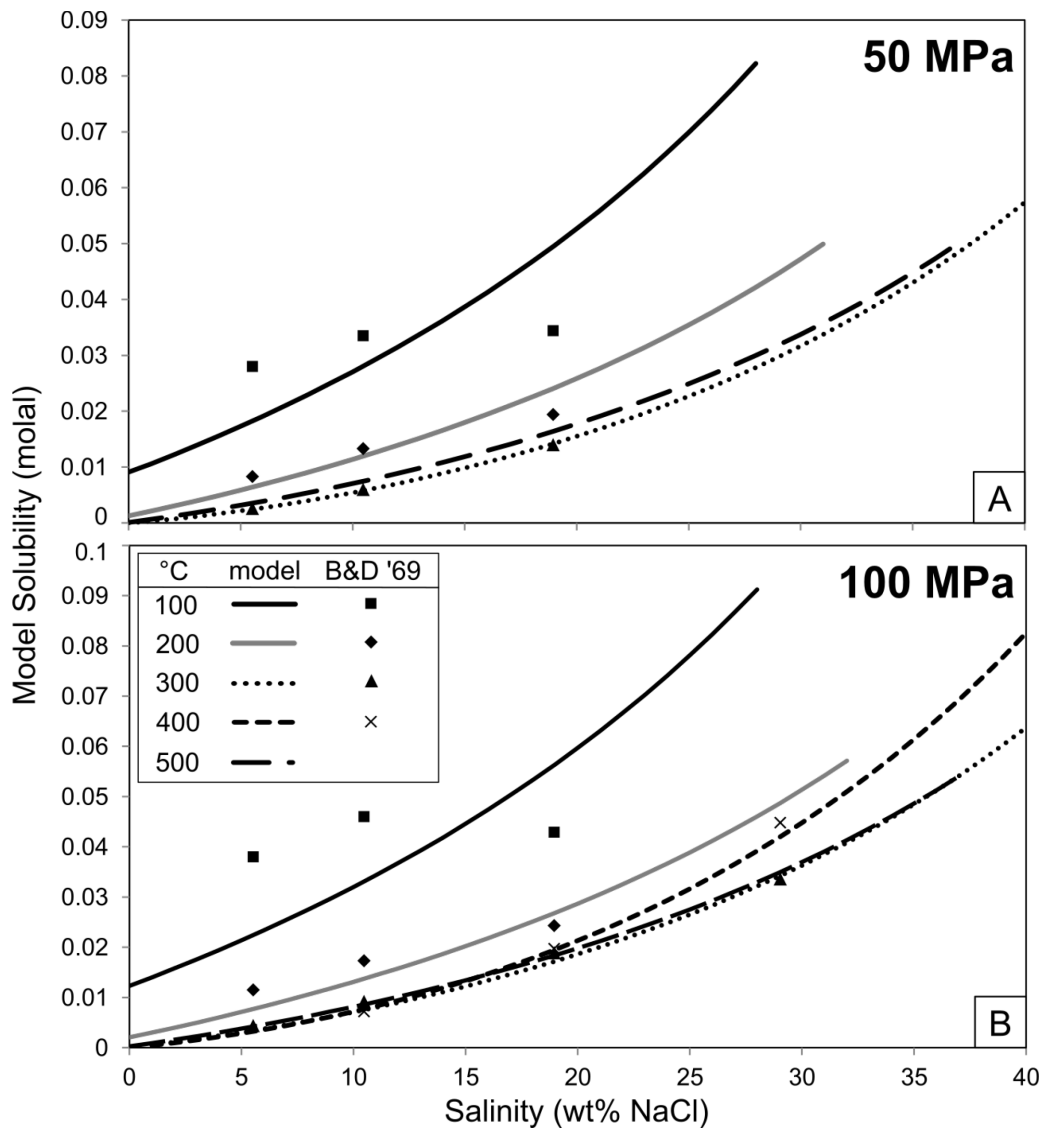


Figure 5. Model solubility of anhydrite (molal) versus fluid salinity (wt% NaCl) at 1000 bar. B&D = Blount and Dickson (1969).

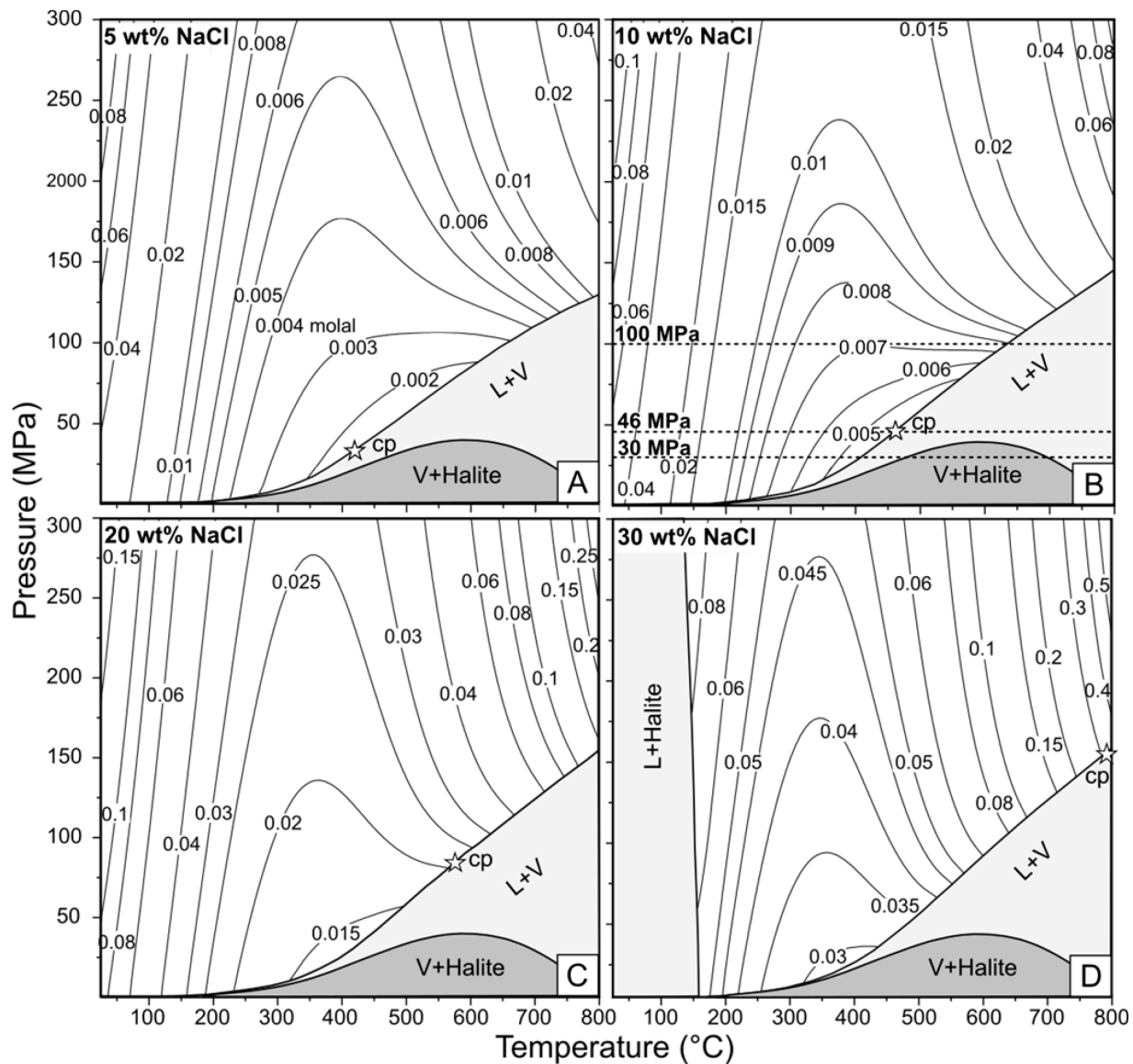


Figure 6. Solubility of anhydrite represented by contour lines in pressure-temperature space. A: solubility contours for a fluid of 5 wt% NaCl. B: solubility contours for a fluid of 10 wt% NaCl. Isobars represent three pressures from Figure 7. C: solubility contours for a fluid of 20 wt% NaCl. D: solubility contours for a fluid of 30 wt% NaCl.

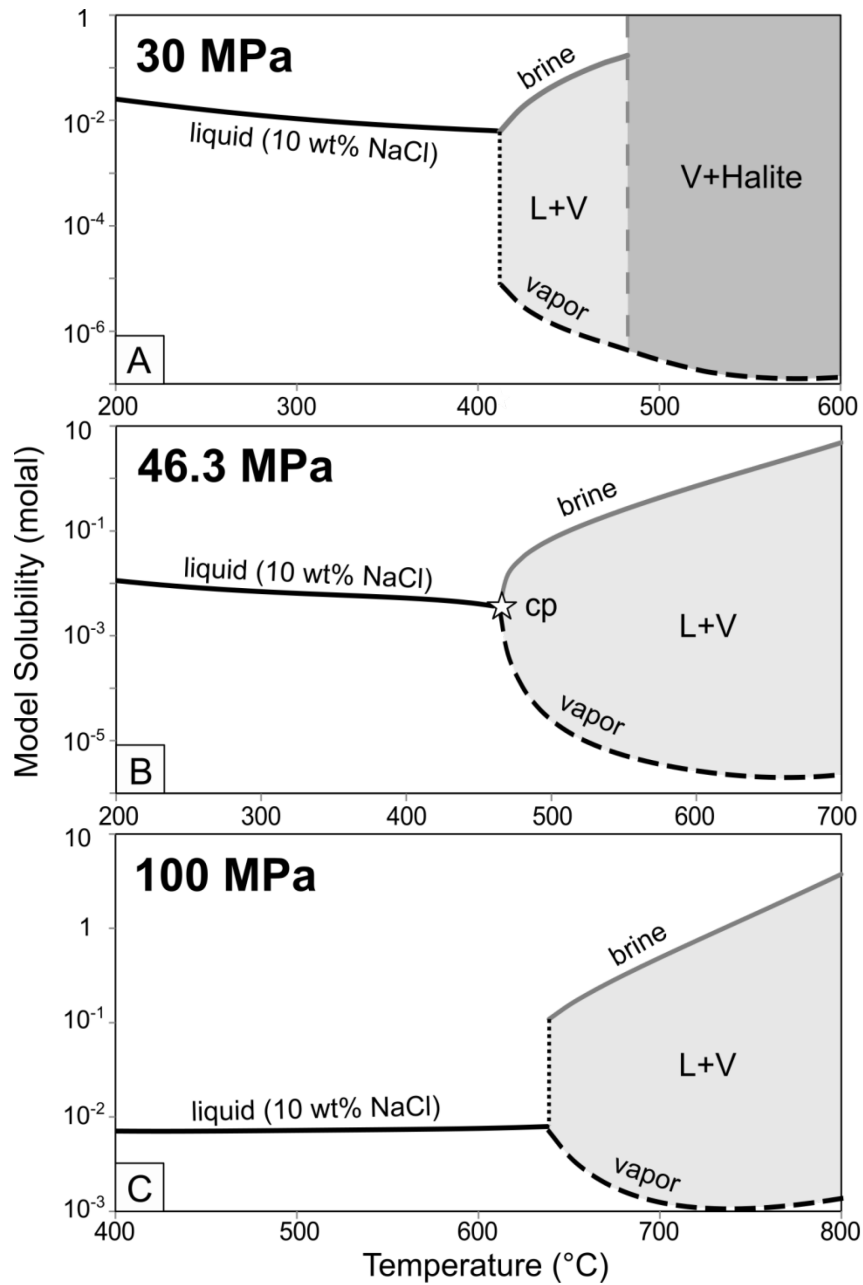


Figure 7. A: Model solubility of anhydrite (molal) versus temperature at 30 MPa. B: Model solubility of anhydrite (molal) versus temperature at the critical pressure (46.3 MPa) for a 10 wt% NaCl fluid. C: Model solubility of anhydrite (molal) versus temperature at 100 MPa. Star indicates the critical point for the fluid.

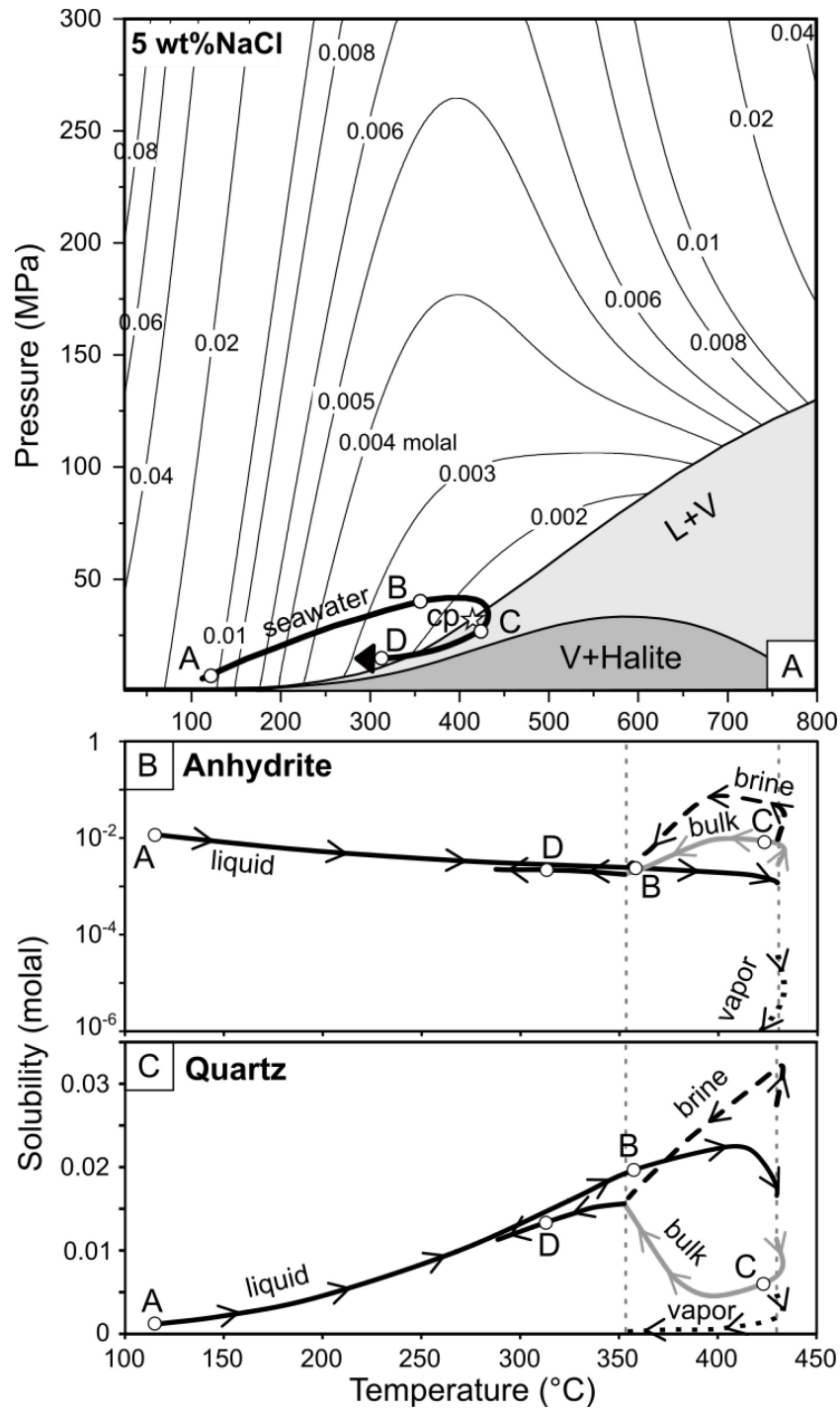


Figure 8. A: A representative fluid flow path for a VMS system (Steele-MacInnis et al. 2021) superimposed on the anhydrite solubility contours for a fluid of 5 wt% NaCl. B, C: Solubility of anhydrite (B) and quartz (C) along the fluid flow path outlined in panel A.

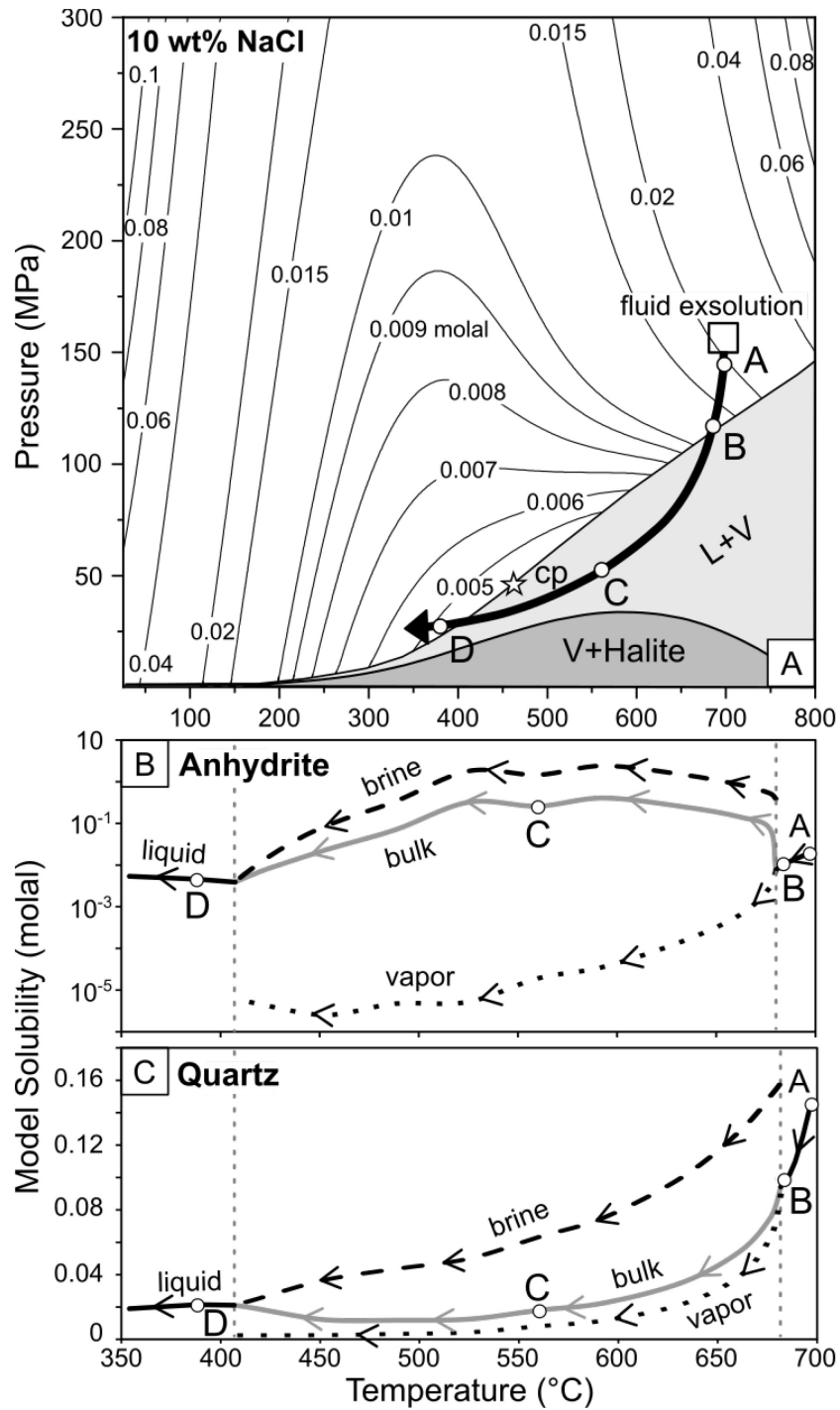


Figure 9. A: A representative fluid flow path for a porphyry system (Steele-MacInnis et al. 2021) superimposed on the anhydrite solubility contours for a fluid of 10 wt% NaCl. B, C: Solubility of anhydrite (B) and quartz (C) along the fluid flow path outlined in panel A.